STUDY OF THE PRESENT-DAY TECTONICS AND SEISMOGENETIC SOURCES OF THE AL-HOCEIMA REGION (MOROCCO) USING GPS AND MTINSAR

Pablo J. González[(1)], Mimmo Palano[(2)], José Fernández[(1)]

[(1)]Instituto de Astronomía y Geodesia (CSIC-UCM), Fac. Cc. Matemáticas, Madrid, 28040 (Spain), Email:pjgonzal@mat.ucm.es; jft@mat.ucm.es
[(2)]Istituto Nazionale di Geofisica e Vulcanologia. Sezzione di Catania, Piazza Roma 2, Catania, (Italy), Email:palano@ct.ingv.it

ABSTRACT

Geodetic analysis and modelling of ground deformation data is a valuable tool that allows constraining present-day tectonics deformation styles and its implications on the related seismic hazards. We re-analyzed the survey GPS data available from the Nubian and Iberian (Eurasian) plate boundary to develop surface strain maps. We also study a high non-linear deformation time series using a multitemporal interferometry synthetic aperture radar (SAR) technique, such as those spanning coseismic signals. That analysis has been challenging due to the problem of intrinsic temporal smoothing of such multibaseline techniques. We used StaMPS/MTI version with the minimum possible temporal smoothing and we retrieve time series of deformation spanning the coseismic signal due to the 24 February 2004, Mw 6.3, Al-Hoceima (Rif, Morocco). Applying a temporal smoothing (atmospheric filtering) to the pre- and postseismic subsets of the time series we obtained a filtered time series that show a persistent signal during the postseismic period.

1. INTRODUCTION

The oblique NW-SE convergence lithospheric plate boundary between Nubian and Iberian (Eurasian) plates is characterized by a diffuse seismicity and deformation distributed along a broad zone of around 400 km (Morocco-Algeria and South Spain-Portugal), bounded by clear sharp linear transpressive to thrusting boundaries to the west (Gloria Fault) and to the east (Northern Algerian margin). Spatial distribution of the predominantly small to moderate strike-to-normal faulting seismicity indicates only a few relatively high seismic areas (Fig. 1). Kinematic behaviour of this major plate boundary using geodetic data is rather sparse [1; 2; 3] and lithospheric deformation style remains poorly constrained, in terms of elastic block deformation tectonics versus diffuse-viscous deformation.

The Al-Hoceima region is considered as the most active seismic area in the Rif Mountains (Northern Morocco) [4]. Two shallow moderate earthquakes occurred in this region in the last 15 years,

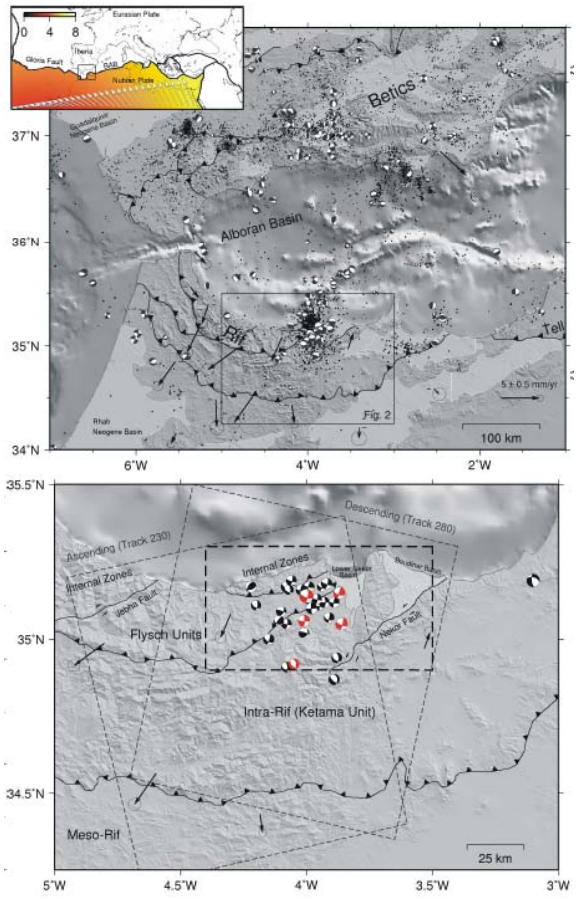

Figure 1. Upper-Panel) Shaded relief map of western Mediterranean Nubia-Eurasian convergent plate boundary (Betic-Rif orogenic arc) region. Seismicity is from IGN seismic catalogue (www.ign.es). Focal mechanisms in black colour from EMMA database (complete for the whole Mediterranean Sea region, $M_w \leq 4$. Black arrows represent GPS velocities (mm yr^{-1}) relative to stable Nubia [13]. Lower-Panel) Location map of the Al-Hoceima region. Gray-coulored focal mechanism corresponding to the 2004 Al-Hoceima seismic serie, red-coulored are the main shock and the 4 largest aftershocks [6].

a Mw=6.0 on 26 May 1994 [4; 5] and a Mw=6.3 on the 24 February 2004 [6]. Previous studies on the 1994 and

Proc. 'Fringe 2009 Workshop', Frascati, Italy,
30 November – 4 December 2009 (ESA SP-677, March 2010)

2004 earthquakes proposed that ruptures occurred on different aparted faults [4; 7; 8; 9]. Some controversies has been opened due to characteristics and orientation of the 2004 earthquake models constrained using geological, seismological and geodetic data [6; 8; 9; 10; 11].

In this paper we analyze the available GPS data and processing ascending and descending acquisitions from ENVISAT satellite to study the moderate magnitude 2004 Al-Hoceima earthquake. We process ASAR data using MTI/StaMPS [12] and we present the results of the inverse modelling of the coseismic and the postseismic signals. Finally, we discussed the results in the light of present-day tectonics of the region.

2. GEODETIC DATA PROCESSING

2.1. GPS data

Kinematic data provided from GPS data analysis at this region is rather poor. The spatial distribution of permanent global networks, as well as the GNSS Spanish national network does not cover properly the plate boundary, so permanent episodically revisited stations are the only available geodetic kinematics data with sufficient spatial distribution to study differential crustal motions [2; 13]. We re-process GPS data by using the GAMIT/GLOBK software [14] and adopting the methodology report bellow. As first step all GPS data were processed by using GAMIT with IGS precise ephemerides and Earth orientation parameters (http://www.iers.org) to produce loosely constrained daily solutions. In a second step, by using the GLOBK software we combine these solutions with global solutions (IGS1, IGS2, IGS3, IGS4 and EURA) provided by the SOPAC, to create a daily unconstrained combined network solution. Finally, by using the GLORG module of GLOBK, these last solutions were analyzed to estimate a long term average velocity in an ITRF2005 reference frame [15] and rotated, as final step, into a fixed Nubian frame (Figs. 1 and 2). The most salient feature in the crustal velocity field is a southwestern escape of the Rif Mountain with respect to the stable Nubia.

By taking into account i) the network geometry, ii) the estimated velocity at each site and iii) the associated covariance matrix C, according to the approach reported in [16] we calculated the horizontal strain-rate field. In particular, assuming that the field is isotropic and homogeneous, a uniform grid is constructed for the area and the velocity gradients are calculated at each node of the grid. All stations in the network are used in the calculation but data from each station are weighted by their distance from the grid node, according to a distance-decaying constant α that specifies how the effect of a station decays with distance from the node. In particular, the weighted version W of C results as function of the site distance according to α:

$$W_{ij} = C_{ij} \exp \frac{\Delta R_I^2 + \Delta R_J^2}{\sigma_D^2} \qquad (1)$$

where i and j are the velocity components corresponding to the I^{th} and the J^{th} stations, ΔR_I and ΔR_J the distances from the I^{th} and the J^{th} stations to the spot to be estimated. The use of the weighting function for C follows an exponential slope allowing the possibility to exclude stations further than a threshold-distance D usually $\geq 2\ \alpha$. In order to achieve realistic results, the strain-rate was computed only in points of a grid which have at least 4 stations in their D-distance neighborhood.

The antisymmetric part of the velocity gradient tensor, w_{ij}, can be easily recast in terms of an axial vector whose magnitude is equivalent to the magnitude of vertical axis rotation rate, or vorticity [17]. The rotations are with respect to a downward positive vertical axis with clockwise positive and counterclockwise negative, as in normal geological conventions.

If the magnitude of shear strain-rates exceeds the magnitude of dilatational strain rate, there are two possible strike directions of faulting that can produce the horizontal components of the strain rate tensor [18]. These are directions of zero length change in the velocity field, and they correspond to the strikes of the two nodal planes in a fault plane solution. In terms of the elements of the strain rate tensor, these strikes are:

$$\tan\theta = \frac{-\dot{\varepsilon}_{xy} \pm \sqrt{\dot{\varepsilon}_{xy}^2 - \dot{\varepsilon}_{xx}\dot{\varepsilon}_{yy}}}{\dot{\varepsilon}_{yy}} \qquad (2)$$

where $\dot{\varepsilon}_{xy}$, $\dot{\varepsilon}_{xx}$, $\dot{\varepsilon}_{yy}$ are the three horizontal strain rate tensor components and θ is the strike angle of the fault measured anticlockwise from the x (east) axis.

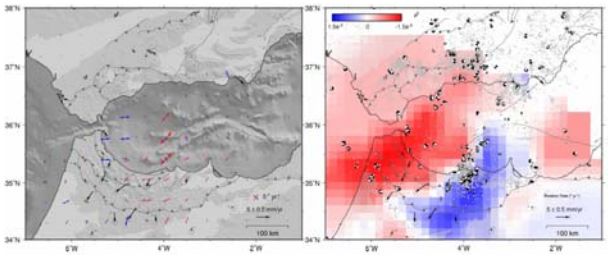

Figure 2. Left-Panel) GPS vector displacements and strain axis computed following the strain computation section. Right-Panel) Finite rotation map, red color indicates clockwise rotations, blue counter-clockwise rotations.

2.2. Radar Interferometry data

Multitemporal or time series analysis algorithms that exploits a relative large number of DInSAR interferograms are useful to retrieve the displacement evolution through time and it is also the preferred adopted solution for the mitigation of atmospheric artefacts, assuming that its effect has a statistical correlation in space and decorrelation in time [19; 20; 21; 22]. Multitemporal DInSAR analysis has been used to study interseismic strain accumulations and postseismic surface motions. StaMPS/MTI can retrieved slow motion processes as well as high non-linear temporal processes [23; 12].

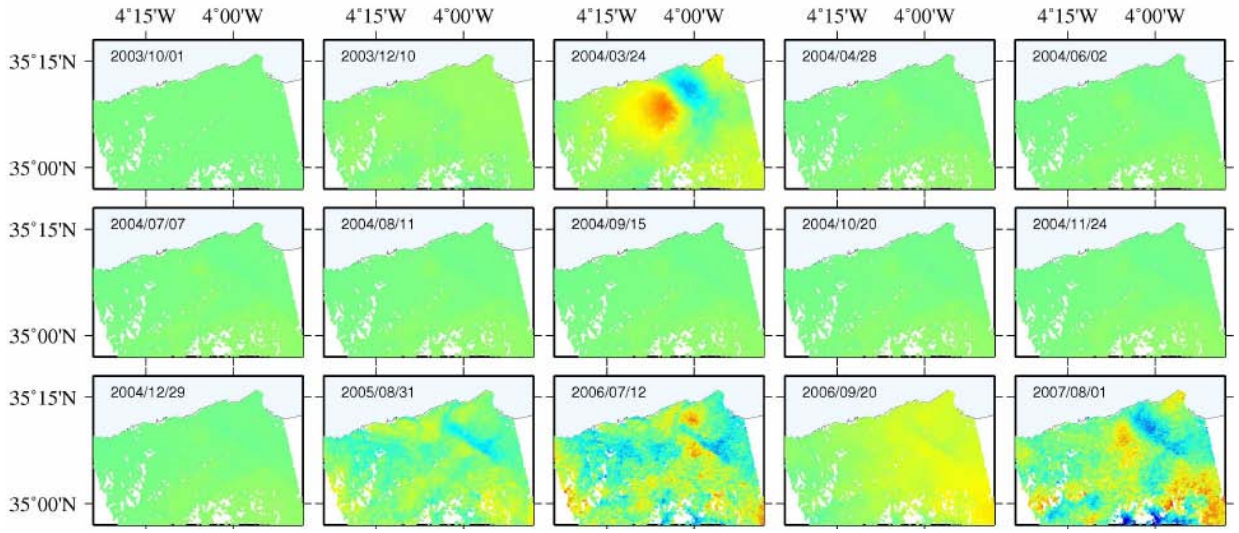

Figure 3. Time series of ascending line-of-sight displacement for Al-Hoceima region between 2003 and 2007. Each image represents the incremental displacement towards the satellite since the time of the previous image, relative to pixels in the northwest corner. Spatiotemporal filtering was carried out in two block using only the pre-earthquake images and subsequently the post-earthquake images. (170422 PS processed, data points)

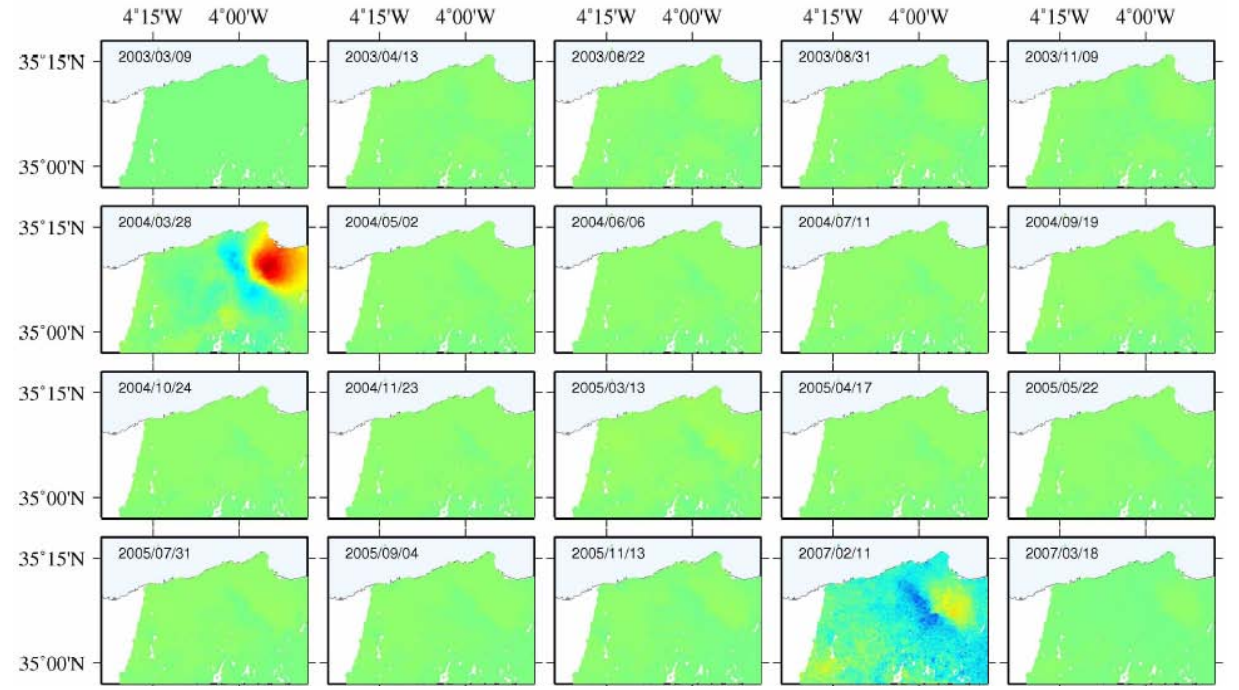

Figure 4. Time series of descending line-of-sight displacement for Al-Hoceima region between 2003 and 2007. Each image represents the incremental displacement towards the satellite since the time of the previous image, relative to pixels in the northwest corner. Spatiotemporal filtering was carried out in two block using only the pre-earthquake images and subsequently the post-earthquake images. (521826 PS processed, data points)

In this paper, we adopted a similar approach to Atzori et al. [24] to minimize the effect of temporal smoothing and also the erroneous propagation of the co-seismic signal over the pre- and post-seismic periods on the analysis of the time series of displacements. First, we have co-registered all SAR images to a common reference image (master image), then we have generated all possible interferograms with small baselines (lesser than 300 meters and also forcing to keep the interferogram dataset to a single subset of connected images), once all interferograms were generated, we run StaMPS/MTI to solve for the unwrapped differential phases and to invert for the time series of displacements. Prior to that point, we have selected all parameters related to temporal smoothing below the maximum temporal sampling rate (typically, 35 days for ENVISAT or ERS satellites). Once the time series of displacements has been generated, we have split the time series into two subsets, separating all pre-earthquake images from post-earthquake images. Finally, to remove the atmospheric noise we have applied to each subset of time series a temporal filter of gaussian type. In this way, we ensure that no coseismic signal is propagated to pre- and post-seismic periods.

The aforementioned methodology has been applied to the selected archived images prior to middle 2007 for ascending and descending passes corresponding to satellite tracks 230 and 280, respectively, for the study of coseismic signal due to the 24 February 2004, M_w 6.3, Al-Hoceima (Rif, Morocco). In Figs. 3 and 4, we show the time series of line-of-sight displacements after orbital de-ramping and temporal atmospheric filtering. Ascending time series analysis is based on the analysis of 33 differential interferograms using 15 SAR images. Descending time series analysis is based on the analysis of 67 differential interferograms using 20 SAR images. The differential interferograms were processed using DORIS software[25].

The descending coseismic signal has a peak-to-through magnitude about 30 cm (Fig. 4), while the ascending data is characterized by a slightly minor magnitude signal (Figure 3). On both descending and ascending time series of displacements (Fig. 3 and 4) shows postseismic signals with magnitudes of around 10% of the coseismic deformation. Note that, the Fig. 3 and 4 do not have the same color scale.

3. DATA MODELLING

3.1. Coseismic modelling

We have isolated the coseismic signal due to the earthquake by differencing pre- and post-event dates on ascending and descending solutions (Fig. 5). In the modelling, first we estimate the geometry of a simple planar fault plane using the finite rectangular dislocation in an half-space [26]. Due to the high-spatial density of the MTInSAR solution spatial subsampling are necessary for the efficiency in the resolution of the inverse problem. We applied a quadtree partition with variance threshold of 0.5 cm. Due to the non-linearly relationship between location and geometric fault parameters and the simulated displacements, a non-linear searching method should be applied (simulated annealing), to obtain the best-fitting set of fault parameters, which minimizes the L2-norm (Tab. 1). Homogeneous slip assumption seems not too realistic, for that reason, we have discretized the dislocation into a series of patches and we resolved for a regularized distributed slip motion over every patch [27].

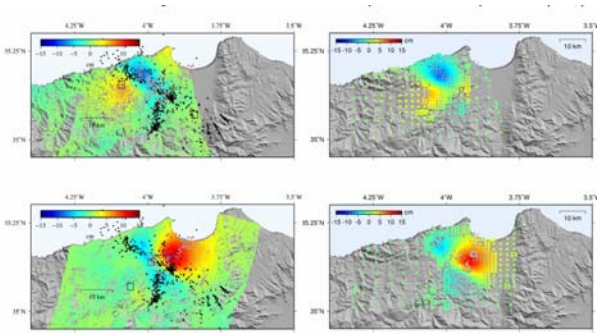

Figure 5. Left column) shows the coseismic full resolution data (up: ascending / down: descending), Right column) is the best-fitting distributed coseismic slip model prediction at the quadtree partition selected points

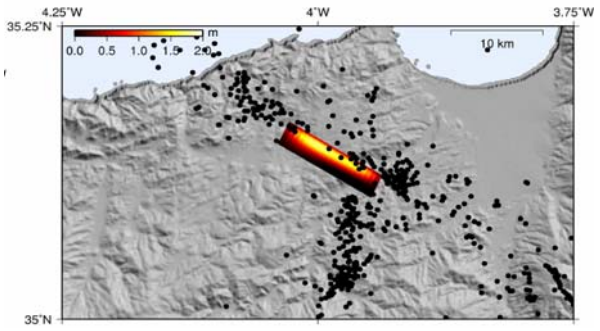

Figure 6. Horizontal projection of the distributed coseismic slip with the aftershocks recorded in the first weeks after the event t [11].

Modelling of the coseismic signal is consistent with previous results based on DInSAR analysis [8; 9; 28]. From distributed slip modelling we can observe that most of the slip is concentrated around 8-10 km depth, with minor to no slip near the surface, which is consistent with the very limited surface faulting [10]. The result also indicates that slip extended shallower on the northwest part of the fault and almost negligible dip-slip occurs as indicate independent seismological results [6].

Table 1. Summarizes results of previous studies on the 2004 Al-Hoceima earthquake (Mo=Moment). [a]Max. distr. slip.

	This Study	Biggs et al., 2006 [8]	Akoglu et al., 2006 [28]	Stich et al., 2005 [6]
Method	MTInSAR	DInSAR + wavefom model.	DInSAR	Moment tensor
Longitude (º)	-3.983	-3.986	-3.993	-4.00
Latitude (º)	35.1445	35.137	35.127	35.14
Depth (Km)	2.8 - 15	2.1 - 18	6 - 10	14
Strike (º)	298.2	295.4	322	106
Dip (º)	78.4	87.4	87	74
Slip (m)	1.00	1.4	2.5[a]	-
Mo (Nm) / Mw	3.65 10^{18} / 6.3	6.2 10^{18} / 6.5	6.6 10^{18} / 6.5	- / 6.3

3.2. Postseismic modelling

We have isolated the postseismic signal due to the earthquake by differencing ascending and descending post-event dates after ~1.5 years (end of 2005). Due to the poor temporal sampling we are not able to unambiguously determine a power-law viscoelastic relaxation behaviour for the post-seismic transient ground deformation (not shown here). We assumed for modelling an approach using an after-(back) slip model, which could potentially reproduce the main features after 1 year of cumulated post-seismic ground motions (Fig. 7).

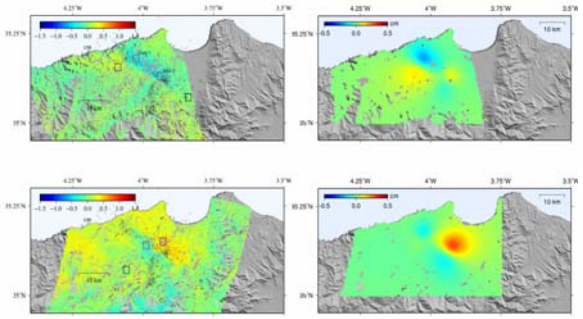

Figure 7. Left column shows the 1-year cumulated postseismic full resolution data (up: ascending / down: descending), Right column is the best-fitting distributed creeping postseismic slip model prediction at the selected points (note the different scale between data – left column and model – right column).

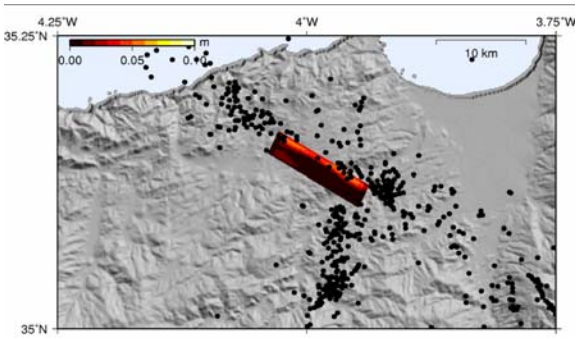

Figure 8. Horizontal projection of the distributed postseismic slip with the aftershocks recorded in the first weeks after the event [11].

Due to the noisier ground deformation data, we applied a homogeneous partition for spatial data subsampling (right panels on Fig. 7). The modelling approach is similar to the coseismic distributed slip model, so we solve for the best-fitting distributed slip model, using the same discretion of the dislocation using the same damping/smoothing factor and dislocation discretization as for the coseismic distributed model (Fig. 8). Although, the post-seismic modelling results can be consider preliminary. Those seem to indicate that aseismic fault creeping following the earthquake concentrates at deeper portions of the fault, where coseismic slip occurred.

4. DISCUSSION

Coseismic ground deformation modelling shows coincidence with previous results based on geodetic data indicating that a major ENE-WSW right-lateral fault ruptured during the 2004 Al-Hoceima earthquake. We found no clear evidence for near N/S-to-NW/SE left-lateral rupture [6; 10]. We also speculate that distribution of aftershocks maybe be dominated by the elastic co-seismic Coulomb stress transfer (Fig. 6), but this hypothesis need also additional calculations. Finally, there is a striking agreement between the azimuths of the 2004 rupture fault and the long-term optimal planes deduced from strain-maps from section 2.1. (Fig. 9). Likely two faults families seem to be active in the Al-Hoceima region a right-lateral NW-SE fault and a conjugated left-lateral NNE-SSW, both consistent with current strain-fields deduced from GPS data.

5. CONCLUSIONS

We use ENVISAR Advanced Synthetic Aperture Radar data to investigate the coseismic and postseismic deformation due to the 24 February 2004, Mw 6.3 Al-Hoceima earthquake. On the basis of the multitemporal analysis of SAR data, we determined the rupture location and developed a coseismic slip model. The inferred rupture location and geodetic moment is in a good agreement with previous studies using classical

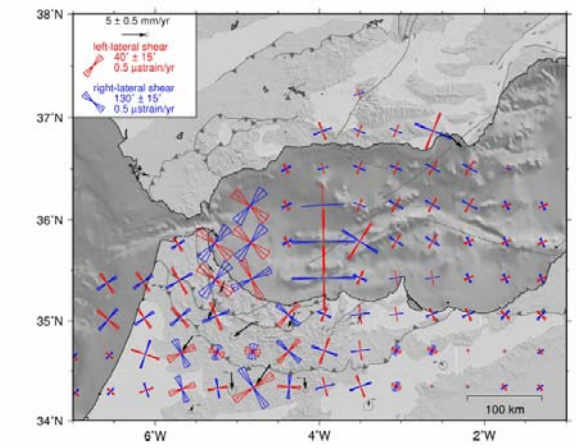

Figure 9. Optimal fault planes deduced from inversion of GPS velocity field. The azimuth axes are scaled according to the maximum shear strain value. In the area south of Al-Hoceima region, note the matching between left- and right-lateral fault planes azimuth from strain maps predictions and the inverted best-fitting azimuth for the 2004 earthquake fault plane.

DInSAR data. The analysis of MTInSAR data during the postseismic period enable us to detect a transient signal over the following 3 years after the event. We developed a post-seismic model to account for the postseismic signal. It is fitted using a model of afterslip in the co-seismic rupture zone. Aseismic slip inversion indicates that slip concentrate in areas bellow the high sliding portions of the coseismic rupture (or asperities) and on the periphery of areas with high coseismic slip at depths of 10-12 km. In the future, we will explore if other postseismic mechanisms (poroelastic or lower crust and upper mantle viscoelastic dynamic relaxation) beneath Al-Hoceima region can contribute significantly to the observed ground deformation. Co-seismic and post-seismic stress relations studies should be investigated in the future to know which mechanisms govern the built-up and relaxation of crustal stresses. Also, geodetic kinematics research works are warranted in the Nubian-Iberian plate boundary to better constrain convergence deformation partition and possible geodynamic models of lithosphere deformation.

Acknowledgements

The radar data in the study were provided by the European Space Agency through Category-1 project CAT-1:4460 ("Geodynamical Studies in the Betic-Rif Ranges by means of Radar Interferometry"). This work was supported in part by the Spanish Ministry of Science GEOMOD (CGL2005-05500-C02) and PEL2G (CGL2008-06426-C01-01/BTE). P.J. González was partially funded by a UCM PhD Thesis Research Fellowship. All figures have been elaborated using the open source software GMT-tools [29].

6. REFERENCES

[1] Nocquet, J.M., and E. Calais (2003) The crustal velocity field in Western Europe from permanent GPS array solutions, 1996-2001. *Geophys. J. Int.*, 154, 72-88.

[2] Fadil, A., Vernant, P., McClusky, S., Reilinger, R., Gomez, F., Sari, D. B., Mourabit, T., Feigl, K., and Barazangi, M. (2006) Active tectonics of the western Mediterranean Geodetic evidence for roll back of a delaminated subcontinental lithospheric slab beneath the Rif Mountains, Morocco. *Geology*, 34(7), 529-532.

[3] Stich, D., Serpelloni, E., Mancilla, F. y Morales, J. (2006) Kinematics of the Iberia-Maghreb plate contact from seismic moment tensors and GPS observations. *Tectonophysics*, 426, 295-317.

[4] Calvert, A., Gomez, F., Seber, D., Barazangi, M., Jabbour, N., Ibenbrahim, A., and Demnati, M. (1997) An integrated geophysical investigation of recent seismicity in the Al-Hoceima region of North Morocco. *Bull. Seismol. Soc. Am.*, 87(3), 637-651.

[5] Bezzeghoud and Buforn (1999) Source parameters of 1992 Melilla (Spain, Mw=4.8), 1994 Alhoceima (Morocco, Mw=5.8) and 1994 Mascara (Algeria, Mw=5.7) earthquakes and seismotectonic implications. *Bull. Seismol. Soc. Am.*, 89, 359-372.

[6] Stich, D., Mancilla, F., Baumont, D. and Morales, J. (2005) Source analysis of the Mw 6.3 2004 Al Hoceima earthquake (Morocco) using regional apparent source time functions. *J. Geophys. Res.*, 110: B06306, doi:10.1029/2004JB003366.

[7] El Alami, S.O., Tadilli, B.A., Cherkaoui, T.-E., Medina, F., Ramdani, M., Ait Brahim, L. and Harnafi, M. (1998) The Al Hoceima earthquake of May 26, 1994 and its aftershocks: a seismotectonic study, Annali di Geofisica, 41, 519–537.

[8] Biggs, J., Bergman, E., Emmerson, B., Funning, G.J., Jackson, J., Parsons, B. and Wright, T.J. (2006) Fault identification for buried strike-slip earthquakes using InSAR: The 1994 and 2004 Al-Hoceima, Morocco earthquakes. *Geophys. J. Int.*, 166: 1347-1362.

[9] Cakir, Z., Meghraoui, M., Akoglu, A.M., Jabour, N., Belabbes, S. and Ait-Brahim, L. (2006) Surface deformation associated with the Mw 6.4, 24 February 2004 Al-Hoceima, Morocco, earthquake deduced from InSAR: Implications for the active tectonics along North Africa. *Bull. Seismol. Soc. Am.*, 96: 59-68.

[10] Galindo-Zaldívar, J., Chalouan, A., Azzouz, O., Sanz de Galdeano, C., Anahnah, F., Ameza, L., Ruano, P., Pedrera, A., Ruiz-Constan, A., Marín-Lechado, C., Benmakhlouf, M., López-Garrido, A., Ahmamou, M., Saji, R., Roldán-García, F.J., Akil, M., Chabli, M. (2008) Are the seismological and geological observations of the Al Hoceima (Morocco, Rif) 2004 earthquake (M=6.3) contradictory? *Tectonophysics*, 475(1) 59-67.

[11] Tahayt A., Feigl K. L., Mourabit T., Rigo A., Reilinger R., McClusky S., Fadil A., Berthier E., Dorbath L., Serroukh M., Gomez F. and Ben Sari D,

(2009) The Al Hoceima (Morocco) earthquake of 24 February 2004, analysis and interpretation of data from ENVISAT ASAR and SPOT5 validated by ground-based observations. *Rem. Sensing Environ.*, 113(2), 306-316, doi: 10.1016/j.rse.2008.09.015.

[12] Hooper, A., (2008) A multi-temporal InSAR method incorporating both persistent scatterer and small baseline approaches. *Geophys. Res. Lett*, doi:10.1029/2008GL034654.

[13] Tahayt, A., Mourabit, T., Rigo, A., Feigl, K.L., Fadil A. and S. McClusky (2008) Present-day movements of tectonic blocks in the Betic-Rif Arc from GPS measurements 1999–2005, *Comptes Rendus Geoscience* 340, 400–413 10.1016/j.crte.2008.02.003.

[14] Herring et al., (2006), GAMIT/GLOBK reference manuals. Massachusetts Institute of Technology, Cambridge, M.A.

[15] Altamimi Z., X. Collilieux, J. Legrand, B. Garayt, C. Boucher, ITRF2005 (2007) A new release of the International Terrestrial Reference Frame based on time series of station positions and Earth Orientation Parameters. *J. Geophys. Res.*, 112, B09401, doi:10.1029/2007JB004949.

[16] Shen, Z.-K., D. D. Jackson, and X. B. Ge, (1996) Crustal deformation across and beyond the Los Angeles basin from geodetic measurements. *J. Geophys. Res.*, 101, 27,957-27,980.

[17] Malvern, L.E., (1969). *Introduction to the Mechanics of a Continuous Medium*, Prentice-Hall, New Jersey.

[18] Haines, A.J., and W.E. Holt (1993), A procedure for obtaining the complete horizontal motions within zones of distributed deformation from the inversion of strain rate data. *J. Geophys. Res.*, 98, 12057-12082.

[19] Ferretti A, Prati C, Rocca F (2001) Permanent Scatterers in SAR Interferometry. *IEEE Trans. Geosci. Rem. Sens.* 39(1): 8–20.

[20] Berardino, P., Fornaro, G., Lanari, R., and E. Sansosti (2002) A new Algorithm for Surface Deformation Monitoring based on Small Baseline Differential SAR Interferograms". *IEEE Trans. Geosci. Rem. Sens.*, 40 (11), 2375-2383.

[21] Mora, O., Mallorquí, J.J. y Broquetas, A. (2003) Linear and non-linear terrain deformation maps from a reduced set of interferometric SAR images. *IEEE Trans. Geosci. Rem. Sens.*, 41, 2243-2253.

[22] Hooper, A., H. Zebker, P. Segall, and B. Kampes, (2004) A New Method for Measuring Deformation on Volcanoes and Other Natural Terrains Using InSAR Persistent Scatterers. *Geophys. Res. Lett.*, 31, L23611, doi:10.1029/2004GL021737

[23] Hooper, A., P. Segall, and H. Zebker, (2007) Persistent Scatterer InSAR for Crustal Deformation Analysis, with Application to Volcán Alcedo, Galápagos. *J. Geophys. Res.*, 112, B07407, doi:10.1029/2006JB004763.

[24] Atzori, S., M. Manunta, G. Fornaro, A. Ganas, and S. Salvi (2008), Postseismic displacement of the 1999 Athens earthquake retrieved by the Differential Interferometry by Synthetic Aperture Radar time series. *J. Geophys. Res.*, 113, B09309, doi:10.1029/2007JB005504.

[25] Kampes, B.M., Hanssen, R.F. and Perski, Z., 2003. Radar interferometry with public domain tools. *In proceedings*: FRINGE 2003, 1-5 Dec, Frascati, Italy.

[26] Okada,Y., Surface deformation due to shear and tensile faults in a half-space. *Bull. Seismol. Soc. Am.*, 75, 1135–1154, 1985.

[27] K.M. Johnson, Y.-J. Hsu, P. Segall, and S.-B. Yu (2001) Fault geometry and slip distribution of the 1999 Chi-Chi, Taiwan earthquake imaged from inversion of GPS data. *Geophys. Res. Lett.*, 28(11), 2285-2288.

[28] Akoglu, A.M., Cakir, Z, Meghraoui, M, Belabbes, S, El Alami, S.O., Ergintav, S, Akyüz, H.S., (2006) The 1994 2004 Al Hoceima (Morocco) earthquake sequence: Conjugate fault ruptures deduced from InSAR. *Earth and Planetary Science Letters*, Volume 252 (3-4), 467-480. doi:10.1016/j.epsl.2006.10.010.

[29] Wessel, P., and W.H.F. Smith, (1998) New, improved version of Generic Mapping Tools released. *EOS Trans. Am. Geophys. Union*, 79, 579.